An Impact-Based and Time-Evolutive Earthquake Early Warning Method.

Aldo Zollo, Simona Colombelli, Alessandro Caruso* and Luca Elia

Department of Physics, University of Naples Federico II

Abstract

Here we propose a methodology for Earthquake Early Warning able issuing the alert based on the real-time estimation of the epicentral area where a ground Intensity measure is expected to exceed a user-set ground shaking level. The method provides in output a P-wave-based, time-evolutive "early" shake map. The P-wave displacement, velocity and acceleration amplitudes are jointly measured on a progressively expanded time window while the earthquake location and magnitude are evaluated using data at near source stations. A retrospective analysis of the 2016, Mw 6.5 Central Italy earthquake records shows that the method naturally accounts for effects related to the earthquake rupture directivity and spatial variability of strong ground motion related to source and path and site effects. Five seconds after the origin time the simulated performance of the system in predicting the event impact is very high: in the 40 km-radius area that suffered an Intensity MCS VIII-IX, 41 over 42 strong-motion instrumented sites would have been successfully alerted, with only one false alert. Even considering the 15-km-radius blind-zone, a 15-55 km wide annular area would have received the alert 2-14.5 sec before the occurrence of the strong ground shaking.

The proposed EEW method evolves with time in a way that it minimizes the missed alarms while increasing successful alarms and to a lesser extent false alarms, so it is necessary for the end-user

* Now at RFI, Rete Ferroviaria Italiana, Rome

to accept these eventualities and account for them in a probabilistic decision scheme depending on the specific safety actuation measure to be undertaken in real-time

1. INTRODUCTION

Earthquake Early Warning Systems (EEWS) are modern, real-time seismic monitoring infrastructures aimed at issuing an alert and activating emergency safety measures to protect people, buildings, and industrial facilities in advance to the impact of strong and potentially damaging shaking waves. The basic principle on which network-based EEWS ground on, is to use the time lag between the alert message issuance and the arrival of damaging seismic waves, to broadcast an alert soon after the first P-waves are detected at a near-source deployed, seismic network. The early warning can reach seconds or tens of seconds in advance the sites to be protected against the arrival of strong shaking waves, depending on the travel distance from the source.

Onsite or stand-alone early warning systems ground on a single stations or small-aperture arrays of sensors deployed in proximity of the target site to secure. In this case, the measures of the initial P-wave amplitude and/or the dominant signal frequency can be used as proxies for the late arriving, strongest shaking wave amplitudes at the same site, with no need for information on the earthquake location and magnitude (*Wu and Kanamori* [2005]). In the cases where a network of stations is deployed in the source area, network-based EEWS analyze the early P-wave signals recorded at the stations, detect the occurrence of the earthquake, determine its location and magnitude and estimate its shaking potential to nearby and distant sites, using previously calibrated empirical attenuation relationships (Ground Motion Prediction Equations, GMPE). The alert notification can reach any distant site within a time interval from the earthquake origin that typically ranges from a few seconds (few tens of kilometers from the source) to several tens of seconds (a hundred kilometers from the source). Different factors may influence the “lead-time”, i.e., the delay between the arrival of the strongest shaking waves at the target site and the first alert time. Among them, the

distance between the source area and the target site, the geometry of the network, the time of event detection, the time needed for the automatic waveform analysis and telemetry and, lastly, the complexity of the source.

During the last two decades EEWS have been widely developed and experimented in several high seismic hazard countries around the world, such as Japan, USA, Mexico, Taiwan, and China (*Allen and Melgar* [2019]). In Europe, several active seismic countries, mostly along the Mediterranean region (Italy, Romania, Switzerland, Turkey, Greece, and the Ibero-Maghrebian region), are nowadays experimenting and testing the use of EEWS mainly for research purposes, while the real-time technology is not yet part of the operational seismic monitoring systems, to be an effective tool for real-time seismic risk mitigation (*Clinton et al.* [2016]).

In Italy, in the frame of an industrial partnership with Rete Ferroviaria Italiana S.p.A. (RFI), the University of Naples, Federico II has recently designed, developed, and implemented a prototype EEW system dedicated to protecting trains and rail infrastructures in a selected segment of the national high-speed railway network, between the cities of Naples and Rome. The system has the main objectives of issuing to the RFI control room the automatic alert for above-threshold strong ground motion amplitudes and, consequently, slowing down/halting the high-speed trains through the activation of Automatic Block Signaling devices along the railway.

Most of the existing EEWS are based on the standard concepts either of the network-based system or of the on-site approach. In some cases, such as in Japan, where the station density and coverage are high and uniform all over the country and where the largest magnitude earthquakes may occur offshore, the nation-wide EEWS benefits from the early P-wave detection at coastline stations (in an on-site approach), for issuing the warning at inland sites. However, the actual integration of the onsite and network-based approaches is under development in Japan, USA and China for providing the output for a timely and robust alert decision scheme.

Along this direction the Japan Meteorological Agency (JMA) is currently testing the propagation of

74 local undamped motion (PLUM) method (*Kodera et al.* [2018]), a wavefield-based EEW approach
75 that predicts seismic intensities directly from spatial inter- and extra-polation of the observed real-
76 time ground motion measures near target sites. When integrated with standard point-source EEW
77 methods, the PLUM method showed an improved performance in terms of more accurate ground-
78 motion prediction for large earthquake rupture and event detection and declaration in case of
79 multiple events sequences.
80 Whichever configuration is used, the standard approaches to EEW are based on simplified
81 assumptions and models both for the earthquake source and wave propagation processes. This may
82 result in highly uncertain predictions of the earthquake impact and therefore in an unacceptable
83 large number of missed or false alarms (*Minson et al.* [2019]).
84 To account for the earthquake source finiteness, different methodologies have been recently
85 proposed and developed to estimate in real-time the fault geometry and size from early P and S-
86 wave signals collected at near-source stations.
87 The FinDer (Finite Fault Rupture Detector) algorithm (*Böse et al.* [2012]), assumes a line source and
88 can automatically detect in real-time its surface projection, the current centroid position, length,
89 and strike, by comparing the real-time ground motion amplitudes to a set of pre-calculated
90 templates, using image recognition techniques. Errors in length estimates are typically on the same
91 order as station spacing in the network so that the method turns out to be useful for accurate
92 earthquake early warnings wherever the station density is sufficiently high.
93 Real-time inversion of amplitudes recorded by high-frequency GPS stations have also been explored
94 to improve the finite fault description in terms of magnitude and source length (*Allen and Ziv* [2011];
95 *Colombelli et al.* [2013]; *Grapenthin et al.* [2014]). In these approaches, the permanent static offset
96 produced by large earthquakes (i.e., the coseismic ground deformation) is inverted in real-time to
97 infer the slip distribution on the fault plane, assuming a prior determined fault orientation. The real-
98 time magnitude and the along-strike extent of the rupture area are finally used to predict the

expected ground shaking due to the finite source.

More recently, the progressive measurement of the P wave displacement amplitude has been proposed to obtain a fast characterization of the extended earthquake source, in terms of magnitude and expected length of the rupture (*Colombelli and Zollo* [2015]; *Nazeri et al.* [2019]; *Zollo et al.* [2021a]). In this approach, the Logarithm of P-wave amplitude vs Time (LPDT curve) is used as a proxy for the Moment Rate Function, allowing for the real-time tracking of the source process evolution and for a rapid characterization of seismic moment and source rupture duration, in the hypothesis of a triangular shape for describing the source process.

Here we present a new methodology that integrates the network and on-site approaches for the alert release. The methodology is based on the real-time, evolutionary mapping of the Potential Damage (or strong shaking) Zone (PDZ) as represented by a predicted Intensity Measure (IM), such as the peak ground velocity/acceleration or the instrumental intensity. The methodology includes the more recent techniques for a refined estimation of the main source parameters (earthquake location and magnitude) that are used to predict the expected ground shaking level at sites not instrumented by strong motion sensors.

Previous studies, in several seismic regions worldwide, have shown that the P-peak initial amplitude is a natural proxy for the late maximum amplitude of seismic records acquired from near-source to regional distance range (epicentral distance < 100 km) (*Wu and Kanamori* [2005]; *Zollo et al.* [2010]). An empirical log-log relationship is usually adopted to correlate the Peak ground motion on the entire signal (in acceleration - PGA - or velocity - PGV) to the initial P-wave peak amplitude (P_a, P_v or P_d), measured in a short time window (1 to 5 s) after the P-wave arrival. These empirical relations have been proposed and used in onsite EEW applications to predict the impact of the potential damaging event, by-passing the estimation of source magnitude and location.

In the proposed method, previous calibrated empirical relations between early P-wave amplitudes and peak ground motion parameters are used to predict the shaking intensities at instrumented,

recording sites. As the P wavefront propagates across the network, a time-varying, *early* shake map is built through a physics-based interpolation approach, which combines the available observed, P-wave and GMPE predicted PGV (following *Worden et al.* [2010]).

Here we validate the proposed methodology through its offline application to the October 30, 2016, M_w6.5 Norcia (Central Italy) earthquake records and discuss the system performance in predicting the earthquake impact.

2. METHOD

The methodology combines specific modules aimed at sequential operations, going from earthquake detection and location to magnitude determination and peak ground shaking prediction. The block diagram of the method is shown in Figure 1, while the detailed theory and implementation of the main steps are described separately in the following sections.

2.1 Earthquake detection and location

The system is designed to process the 3-component, ground acceleration records, as acquired by a real-time, dense network deployed in the earthquake epicentral area and extending to local and regional (100 km) distances. The first P-wave arrival time signals are detected by the real-time Filter-Picker 5 algorithm (*Lomax et al.* [2012]) on the vertical component of the acceleration waveforms.

As soon as the first two stations have triggered the event, a real-time location estimate is obtained by using a real-time version of the M-PLOC algorithm described in *Zollo et al*. [2021b]. M-PLOC provides a probabilistic solution for the earthquake location, based on the real-time measure of three different observed quantities (differential arrival times, amplitude ratios, and back-azimuth from the P-wave polarization) evaluated in progressive (or fixed) time windows after the first P-wave arrival. The most probable estimates of hypocenter coordinates and origin time are provided as soon as the first stations trigger the event and are progressively updated as the P-wave front expands

149 across the network and new portions of signals are acquired by more and more distant stations. In
150 the present application only the differential arrival times at pairs of stations within the network have
151 been used for earthquake location, since preliminary tests confirmed that the azimuthal coverage
152 of stations was sufficiently dense to get optimal location without using additional parameters.
153 When using only differential P-arrival times, the M-PLOC method determines the earthquake
154 location as the maximum likelihood location contained in a gridded 3-D crustal volume. A minimum
155 of 2 stations where the first P-arrival is detected are used to get the first earthquake location. In this
156 case the epicenter location is set at the half-length of the surface segment joining the two station
157 locations and a trial-depth value is assumed. In the considered application a trial-depth of 10 km has
158 been set based on the historical seismicity of the area. With three or more stations at which the P-
159 arrival is detected, the mutual differential times allow to constrain the hypocenter location with an
160 accuracy that is progressively improved as more P-arrival times are available from the automatic
161 picking. Details about the earthquake location uncertainty estimates inferred from the PDF
162 distribution can be found in Zollo et al. [2021b].
163
164 *2.2 Peak parameter measurement*
165 Starting from the P-wave arrival time, we measure the initial peak amplitude parameters, P_a, P_v and
166 P_d, as the absolute, maximum value of the vertical component of acceleration, velocity and
167 displacement, respectively. The measures are repeated every 0.5 sec and are stopped at the
168 expected arrival of the S-waves, as predicted by the earthquake location. The acceleration records
169 are first processed by removing the mean value and the linear trend. Waveforms are then integrated
170 once to obtain velocity waveforms and the linear trend is removed again, prior to measure P_v. A
171 second integration is performed to get displacement traces, followed by a causal, high-pass
172 Butterworth filter, to remove the artificial low-frequency drifts and baselines on displacement
173 traces, which may appear from the double integration operation (*Boore et al*. [2002]). Following the

approach already used by *Caruso et al.* [2017], we automatically select the proper cut-off frequency for the filter, which can be either 0.075Hz or 1Hz, depending on the quality of the input data, as briefly recalled in the following lines. Two parameters are used to evaluate the quality of data: the signal-to-noise ratio (SNR) and the P_d/P_v ratio. Specifically, the SNR is computed as $SNR = 20 * log10(P_d/{P_d}^N)$, where P_d is measured on the available signal in the selected time window and ${P_d}^N$ is the maximum displacement of the pre-event noise, over the same time window. As for the P_d/P_v ratio, both peak amplitude parameters are measured in the same time window. Based on the idea that P_d and P_v follow a linear, constant-coefficient empirical relation with magnitude and logarithm of hypocentral distance, their ratio is therefore expected to vary in a predetermined range around a constant level. On the contrary, out-of-range P_d/P_v values indicate noisy data, with the peak displacement possibly contaminated by artificial long-period distortions. The observed values of SNR and of the P_d/P_v ratio are therefore compared to predetermined threshold values, for the automatic selection of the proper filter, or data are eventually discarded if the quality control is failed (see *Caruso et al.* [2017], for further details).

2.3 Magnitude estimation

In our method the real-time moment magnitude (Mw) is obtained by averaging the single magnitude estimates derived from the three P-peak amplitude parameters (P_a, P_v and P_d), measured at the near-source stations. Given a recording station at hypocentral distance R, for each parameter, we use an empirical attenuation relationship to estimate the moment magnitude, of the form (*Wu et al.* [2006]; *Zollo et al.* [2006]):

$$M_w^x = A_x \cdot \log P_x + B_x \cdot \log R + C_x \quad (1)$$

where $x = a, v, d$ indicates acceleration, velocity and displacement P-waveform records, and coefficients A_x, B_x and C_x are determined by a linear regression analysis using an existing earthquake data set in the region of interest. Details about the calibration dataset are reported in

Text S1 of the Supplemental Material. The empirical regression coefficients (A, B, C) and their uncertainties are reported in Table S1 of the Supplemental Material, together with the standard error of the regression, while plots of calibration data and scaling relationships are shown in Figures S1 and S2 of the Supplemental Material.

For a given station i and for each time step t, the magnitude value is obtained by the weighted average of all the available predictions:

$$M_w^{it} = \frac{w_a \cdot M_w^a + w_v \cdot M_w^v + w_d \cdot M_w^d}{w_a + w_v + w_d} \quad (2)$$

where the weights w_x are estimated from the standard errors σ_x' of empirical relations (1) as $w_x = \frac{1}{\sigma_x'^2}$. Finally, considering that at the time step t, a total of N stations has recorded the P-wave signal with a variable signal length T_d^{it} (i is the station index), the final, average magnitude is obtained as:

$$M_w^t = \frac{1}{\sum_1^N T_d^{it}} \sum_{i=1}^N T_d^{it} \cdot M_w^{it} \quad (3)$$

where the signal length T_d^{it} is used to weigh the station-magnitude values. Here we assume that the estimates inferred from larger portion of P-wave signals must have a larger weight than those obtained from shorter time windows. In our approach, the magnitude is computed using only stations that satisfy a specific criterion, as explained below.

A previous study (e.g., *Colombelli et al.* [2015]) has shown that the joint use of the three P-peak amplitude parameters allows improving the accuracy and reducing the uncertainty on magnitude estimation, especially when a limited time window and number of stations are available for the measurement. Furthermore, initial P-wave observation of real earthquakes have shown that when expanding the time window, the three peak amplitude parameters generally increase with time. The typical Logarithm of P-peak Displacement vs Time (LPDT) curve starts from small values and reaches a stable plateau level at a corner-time that depends on the final event magnitude (*Colombelli et al.* [2012; 2014]; *Trugman et al.* [2019]). Additionally, *Colombelli and Zollo* [2015] observed the dependency on magnitude of this corner-time and used it to estimate the fault length of earthquakes

in Japan. *Nazeri et al.* [2019] and *Trugman et al.* [2019] confirmed this general behaviour of LPDT curves by analyzing extended data-sets for Japanese and Central Italy earthquake sequences. More recently, *Zollo et al.* [2021a] propose a technique to determine the rupture radius of a circular earthquake rupture from the estimations of the corner-time of azimuthally averaged LPDT curves.

Given the general increasing amplitude of initial P-wave peak parameters with time, reliable magnitude estimates can be obtained only for P_x values measured at the plateau of the curves, while significant magnitude underestimations can generally occur using shorter time windows (i.e., while the curve is still increasing). In our method, to avoid the initial underestimations, we developed an automatic algorithm able to identify the plateau time of the curves, by continuously monitoring their time derivative and evaluating when it reaches a near-to-zero threshold value. At this time, i.e., when the plateau has been reached, the corresponding peak parameters start being used for the magnitude determination. It is worth to note that the three curves (LPAT, LPVT, and LPDT) are expected to reach the plateau level nearly at the same time (*Colombelli et al.* [2014]; *Nazeri et al.* [2019]), thus, for computational simplicity, we only monitor the time derivative of the LPVT curve. Figure 2 shows some examples of recorded seismograms (in acceleration) at a few stations around the epicenter and the corresponding computation of LPDT curves, which are available at sequential times, as the P-wave front propagates across the array. Finally, to ensure a rapid convergence to the final magnitude of the event, only the recordings within 100km from the epicenter are used for the magnitude computation, or alternatively a maximum of 30 triggered stations.

2.4 Computation of the "Early" Shake-Map

With the aim of building real-time reliable, P-wave based, shake maps, we predict the peak ground motion in the region of interest using two different approaches, one for the recording sites and another for the *virtual* nodes, i.e., the not-instrumented grid nodes. Specifically, the Peak Ground Velocity (PGV) at the recording sites is predicted from the recorded P-amplitudes of the early P-wave

signals using eq. 4. The PGV at the *virtual* nodes is instead predicted through a physics-based interpolation techniques which uses the available regional ground motion prediction equation (GMPE) and real-time estimates of earthquake location and magnitude. The two approaches are described in detail in the following sections.

2.4.1 Peak ground motion prediction at the recording sites

Like what has been done for the magnitude, the three peak amplitude parameters P_a, P_v and P_d measured at the recording sites for each time window t, are jointly used to predict the expected PGV, based on a scaling relationship of the form:

$$\log PGV_x^t = D_x \cdot \log P_x^t + E_x\,; \qquad w_x = \frac{1}{\sigma_x^2} \quad (4)$$

Where D_x, E_x are the empirically estimated coefficients and σ_x are the standard errors of the scaling relationship between the PGV and the P_x parameter. Coefficients D and E are empirically estimated using a linear regression analysis, for each peak amplitude parameter (P_x) and each time window (t). An example of data and linear regression for the 3-s time window is shown in Figure S3 of the Supplemental Material, while the full list of estimated coefficients (and their uncertainties) is reported in Table S2 of the Supplemental Material. The predicted value of $\log PGV$ and its uncertainty at any time t are therefore obtained as the weighted average of the three estimated $\log PGV_x^t$ values:

$$\log PGV_{onsite}^t = \frac{w_a \cdot \log PGV_a^t + w_v \cdot \log PGV_v^t + w_d \cdot \log PGV_d^t}{w_a + w_v + w_d} \quad (5)$$

$$\sigma_{logPGVonsite} = \sqrt{\frac{w_a \cdot \left(\log \frac{PGV_a^t}{PGV_{onsite}^t}\right)^2 + w_v \cdot \left(\log \frac{PGV_v^t}{PGV_{onsite}^t}\right)^2 + w_d \cdot \left(\log \frac{PGV_d^t}{PGV_{onsite}^t}\right)^2}{w_a + w_v + w_d}} \quad (6)$$

Coefficients D and E of equation (4) are region-specific and must be preliminary determined through analyses that use data from past earthquakes recorded in the region of interest. Furthermore, the

algorithm is designed to monitor both the vertical and the horizontal components. The predicted PGV from the vertical P_x amplitude is continuously compared to the PGV value measured on the horizontal components. At any time along the waveform, the maximum between these two values is used as the peak ground motion estimate.

At the end of the event (set at fixed time window of 30 seconds after the first P-wave arrival in our application) for each seismogram, the final PGV measured as the maximum of the NS and EW horizontal components, replaces the last P-wave predicted one, so that the evolutive, "early" P-based, PGV predictions naturally converge toward the final PGV values.

2.4.2 Peak ground motion prediction at "virtual" nodes

At each time step t, the prediction of PGV at the not-instrumented sites of the grid map, is obtained using a physics-based, interpolation algorithm combining the available information collected by stations that recorded the early portion of P-wave signal at the time t:

1) PGV_{onsite}: the PGV predicted at network stations from P-peak amplitudes through equations (5) and (6);

2) PGV_{GMPE}: the PGV predicted by a regional GMPE given the available estimates of earthquake location and magnitude. In our applications we used the GMPEs derived by *Bindi et al.*[2011] for Italy.

With the same approach as used for the shake-map computation (*Worden et al.* [2010]), our algorithm combines these two pieces of information through the following relationships:

$$PGV^t(x,y) = \frac{\sum_{i=1}^{N}\left[\frac{1}{\sigma_{onsite}^{i2}} \cdot PGV_{onsite}^{i}\right] + \frac{1}{\sigma_{GMPE}^{2}} PGV_{GMPE}(x,y)}{\sum_{i=1}^{N}\left[\frac{1}{\sigma_{onsite}^{i2}}\right] + \frac{1}{\sigma_{GMPE}^{2}}} \quad \text{for all station } i \text{ with } r_{\Delta} > 0 \quad (7)$$

where:

$$\sigma_{onsite}^{i} = \sigma_{PGV} \cdot \left(1 - \exp\left(-\sqrt{0.6 \cdot r_{\Delta}}\right)\right) \quad \text{for } r_{\Delta} \leq R_{roi}$$

$$\sigma_{onsite}^{i} = \left(\sigma_{onsite}^{i} \middle| r_{\Delta} = R_{roi}\right) \cdot \frac{r_{max} - R_{roi}}{r_{max} - r_{\Delta}} \quad \text{for } r_{max} \geq r_{\Delta} > R_{roi} \quad (8)$$

$$\sigma_{onsite}^{i} = \infty \quad r_{\Delta} \geq r_{max}$$

with:

- $PGV^{t}(x, y)$, the PGV predicted at the virtual node located at (x, y);
- r_{Δ} , the distance between the i-th network node and the virtual node;
- σ_{GMPE} , the standard error of the used GMPE;
- σ_{PGV}, the standard error of the P-wave predicted PGV retrieved from equation 4;
- R_{roi} (roi=region of influence), the distance of the area around the network stations where the observed data influence the PGV interpolation more than the PGV estimate through the GMPE (PGV_{GMPE});
- r_{max} , the limiting distance of the area where the observed data influence the interpolation.

The interpolation formula of equation (7) is valid for all points (x,y) at the surface, except for those where stations are located, where the predicted PGV is obtained from equation 4.

Starting from the first P-wave arrival time, equations (7) and (8) allow predicting the PGV and its uncertainty at any point of the area surrounding the epicenter. This PGV value is expected to vary with time as new data become available from stations located at increasing distances from the epicenter and to finally stabilize at a constant value for a high number of station amplitude data and wide P-wave time windows. We note that the maximum P-window length is chosen according to the expected S-arrival time, which is the same criterion used to determine the empirical relations (4).

The final output is the predicted PGV *vs.* time at any position (x,y) around the earthquake source, which can be finally converted to instrumental intensity through regional empirical relations (e.g. *Faenza and Michelini* [2010], for Italy) to be included in the early warning alert broadcast message.

3. Application to the Mw 6.5, October 30, 2016, Norcia (Central Italy) earthquake

To validate the proposed early warning method and evaluate its performance, we performed an off-line application, by simulating the real-time data streaming of the 2016 October, 30, Mw 6.5 Norcia (Central Italy) earthquake (Figure 2). The event was caused by the activation of an about 20 km long system of two normal faults along the Central Apennine chain, rupturing two main slip patches (peak-slip ~3 m) and producing a strong ground shaking and severe building damage and collapses in a wide area extending over 50 km distance around the epicenter (*Scognamiglio et al.* [2018]). According to *Scognamiglio et al.* [2018] the rupture nucleated at about 9 km depth and propagated up-dip and south-eastward along the N155°E fault with a rupture velocity of 2.8 km/sec and then triggered a secondary rupture on a smaller fault, 10 km southern of the main fault epicenter, with a clockwise rotated strike direction (N210°E). The two rupture episodes produced average fault slips of 0.4 and 0.6 meters with seismic moments $5.9 \times 10^{18}\ Nm$ and $2.9 \times 10^{18}\ Nm$, respectively. The maps of strong ground shaking (expressed in MCS intensity scale, Peak Ground Velocity and Peak Ground Acceleration) are reported in the November 2016 INGV Working Group' report (*Gruppo di Lavoro INGV*, [2016]). The maps are computed using the peak ground shaking data available from the European Strong Motion database (*Luzi et al.* [2016]) containing the earthquake waveforms from a total set of 240 stations with a maximum epicentral distance of 673 km. The shaking intensity reported in the map ranges from IV to IX, with the level of VI, corresponding to "strong perceived shaking" in the MCS scale (PGA of 4.8 %g and PGV 2.4 cm/sec), affecting a wide portion of the Central-Italy territory and extending over an area of about 100 km radius out of the epicenter.

For our simulation, we used the three component earthquake records acquired by 60 stations of the Italian Accelerometric Network (RAN) located within an area of 50 km radius centered at the event epicenter (Figure 2). The selected sub-network provides a rather dense azimuthal and distance coverage of the source with an average inter-station spacing of 15-20 km.

Figure 3 shows the time changes of the location error (distance in km from the INGV bulletin solution) and moment magnitude, using the P-wave arrival times and peak amplitudes available at

each time step, as the P-wave front progressively expands across the network. In the EW method these data are used to update the PGV predictions at virtual nodes (eq.7) using the specific GMPE for Central Italy. The moment magnitude estimated by the EW method is generally smaller (first estimate, Mw 5.6, late estimate Mw 6.2) relative to offline measures using regional and teleseismic S and surface waves (6.5+) while it is better consistent with Mwp (6.3) but still underestimated. In this case, the difference of -0.1 between the EW-Mw and Mwp can be attributed to the shallower hypocentral depth (about 6 km, relative to the bulletin depth of 9 km) determined in RT by the EW method using only near-source P-wave arrival-times. We note that despite the underestimation of the final earthquake depth and moment magnitude, as discussed later in this article, the EW method can predict and track with great accuracy the peak ground shaking area, this information being used for early warning.

Figure 4 shows the space-time evolution of the P-wave-based prediction of instrumental intensity (I_{MM}) (derived from PGV though the empirical relations of *Faenza and Michelini* [2010]). Snapshots are shown at different times from the event origin time.

The Potential Damage Zone (PDZ) is here defined as the area where the predicted maximum intensity $I_{MM} \geq VII$. The PDZ is observed to clearly expand with time, changing its shape and extent, as new data from the P waves propagating across the array are available. At its initial stage (4-5 sec, Figure 4a,b) the PDZ assumes a near-circular shape, since it is totally controlled by the GMPE-predicted PGV, with the contribution of only few near-source stations. At larger times (10-30 sec, Figure 4c,d,e) the PDZ depicts a nearly elliptical area with a predominant elongation to south-east of the epicenter. The anisotropic shape of the PDZ is the effect of larger P-wave and PGV-predicted amplitudes toward the South-East direction which is consistent with a dominant SE earthquake rupture propagation, as revealed by the kinematic source modelling of near-source strong motion and GPS records (*Cheloni et al.* [2017]).

A precautionary first alert could be issued to the whole region of interest at the time of the first alert

(around 4 sec) when a ground shaking of $I_{MM} \geq VII$ is predicted to affect a wide near-circular area (radius 30 km) around the epicenter.

After about 15-20 seconds from the first P-arrival at the network, the shape of the PDZ remains stable and unchanged even adding the contribution of more distant stations (Figure 4d,e). A qualitative comparison of the 15 sec "early" shake-map (Figure 4d) with the final released by INGV (Figure 4f) shows a very good matching of $I_{MM} > VII$ areas between P-wave predicted and final ground shaking maps. In particular, the rupture directivity toward SE is evident from the shape of the PDZ dominantly elongated in this direction.

We define the "time of the first alert" (T_{FA}) as the time measured from the origin time (OT), at which the first PGV (IMM) prediction overcomes the threshold for the alert, that has been set to PGV=3.9-4 cm/sec for IMM=VII, following the scale proposed by *Faenza and Michelini* [2010]. In our simulated scenario, T_{FA}=3.6 sec, which accounts for the P-wave propagation from the earthquake depth to the surface and for the time required to get to the plateau level of LPDT curves at the two stations nearest to the epicenter.

The early warning system performance for this single earthquake scenario can be assessed as the ability of the system to predict the earthquake impact (IMM, instrumental intensity above the threshold) in terms of the number of successful (positive and negative), missed and false alerts.

In detail, we can define the following criteria:

Successful Alert (SA): $I_{MM}^{pred} \geq I_{MM}^{thre}$ & $I_{MM}^{obs} \geq I_{MM}^{thre}$ (9a)

Successful No-Alert (SNA): $I_{MM}^{pred} < I_{MM}^{thre}$ & $I_{MM}^{obs} < I_{MM}^{thre}$ (9b)

Missed Alert (MA): $I_{MM}^{pred} < I_{MM}^{thre}$ & $I_{MM}^{obs} \geq I_{MM}^{thre}$ (9c)

False Alert (FA): $I_{MM}^{pred} \geq I_{MM}^{thre}$ & $I_{MM}^{obs} < I_{MM}^{thre}$ (9d)

where $I_{MM}^{thre} = VII$

We evaluate the performance of the EEW method at times T_{FA}=3.65sec, $T_{FA} + 0.5\ sec$ (4.15 sec) and $T_{FA} + 1.5\ sec$ (5.15 sec), all times evaluated since OT (Figure 5). Indeed, we expect that the

performance of the system should improve as a function of the time, since additional recorded P-amplitudes become available and more accurate estimations of the earthquake location and magnitude are derived from distant stations.

Figures 5a, b and c show the performance of the system at the three different times in terms of SA (dark green), SNA (light green), MA (red) and FA (yellow) with colored circles at the station locations. At 3.65 sec after OT (Figure 5a), the percentage of successful alerts (SA+SNA: 57%) is slightly higher than missed/false alerts (MA+FA: 43%) considering the whole area covered by the seismic network, while it reaches near 71% when considering epicentral distances smaller than 40 km. Indeed, at this time, the majority of missed alerts are issued at the largest distances from the epicenter (R > 30-40 km).

Half a second later (Figure 5b), the impact prediction performance highly improves, with an overall increase of the percentage of successful alerts (both SA and SNA), reaching 92%, when considering the whole 55 km radius area. At this time, a single SNA and MA are recorded, with 4 FA (6.6%). Within a circle of 40 km epicentral radius we measure 98% of SA with just one FA at a station not far from the circle. At TFA+1.5sec the system performance evolves to a condition where only SA (92%) and FA (8%) are recorded. All FAs except one are recorded at outside the 40 km radius, where all sites still record all SAs except a single FAs.

The change with time of the relative proportion of SA, SNA, FA and MA is a typical effect of our evolutive early warning systems that will be discussed later in the paragraph “Discussion”.

Concerning the lead-times, these are estimated as $T_{LT} = T_S - T_{FA}$, where T_S is the predicted S-wave arrival time given the earthquake location and the average crustal velocity values (V_P=5.5 km/s; V_S=3 km/sec) for the area. The map of lead-times (Figure 6) shows values ranging from 2 s to 14.6 sec at 15 km and 55 km from the epicenter, respectively. For the considered event and station distribution the *blind-zone*, e.g., the area where the first S-waves are expected to arrive before the alert is issued, covers a circular surface with a radius of 6.5 km centered at the epicentral position.

Discussion

We propose a new earthquake early warning method where the alert is issued based on the progressive tracking of the potential damage zone (depending on the chosen PGV/IMM threshold) which is mapped using a predicted PGV value resulting from the physics-based interpolation of the recorded P-amplitude and GMPE-derived PGV values. The GMPE values are determined using the earthquake location and magnitude estimated by near source recording of early P-wave signals. An update of PGV/IMM predictions is done as new locations and P-wave data are available from more distant stations. Since it is based on the recorded ground motion P-amplitudes at stations around the epicenter, the proposed technique naturally accounts for the spatial variability of strong ground motion related source (i.e., rupture directivity), crustal wave propagation and site amplification as inferred from the early P-signals.

The onsite PGV at instrumented sites is predicted from the P-peak acceleration, velocity and displacement values measured on the original vertical component record. In this study, the empirical relations log PGV vs log (Pd, Pv, Pa) have been determined and calibrated for the Central Italy region using the available waveform databank for previous earthquakes in the magnitude range 3-6.5 and distance interval 10-100 km.

The use of the three P-amplitude, observed parameters showed to improve, in general, the accuracy of the predicted PGV relative to the use of a single parameter, since they carry on information about the P-amplitude in different frequency bands. In addition, since the P-peak amplitude for moderate-large earthquakes is expected to increase with time from the first P-arrival, the method implements an algorithm allowing to start measuring the P-amplitude only after the LPDT curves reach their plateau. This would make more robust the technique by reducing the number of missed alerts at the expenses of a longer P-wave time window to explore. Recently *Colombelli et al.* [2014, 2020] showed that the initial slope of the LPDT curves scales inversely with the earthquake magnitude, suggesting

445 that this initial slope parameter could be used as a proxy for the rapid assessment of the earthquake
446 size during an ongoing rupture. Future developments of the described method will include initial
447 slope measurements to provide constraints on the ongoing event magnitude, to be used for a faster
448 time of the first alert.

449 The off-line application of the EW method to the M 6.5 October,30, 2016 Norcia earthquake in
450 Central Italy shows the reliability and robustness of the methodology. It provides a rapid alert
451 message with a time-varying assessment of the earthquake impact as obtained by the algorithm of
452 data interpolation able to build a realistic, P-wave-based, "early" shake map. We showed that the
453 latter is very consistent with the shake-map computed by INGV tens of minutes after the earthquake
454 occurrence, using the recorded PGV data on the horizontal components at strong motion stations
455 over a wide distance range.

456 The considered scenario case confirms a good performance of the system in terms of reliability of
457 the predicted intensity map which naturally includes the spatially variable ground motion shaking
458 as originated by source directivity effects, although inferred from near-source recorded P-
459 amplitudes. This is already visible on maps after few seconds from the first P-wave recorded at the
460 near-epicenter stations.

461 The rapidity of the system to process the data and release the warning along with the reliability of
462 ground shaking predictions critically depend on the network density and azimuthal coverage in the
463 epicentral area.

464 We showed that the capability of the EW system to predict the strong motion above the threshold
465 improves with time. Only 1.5 sec after the TFA (5.15 sec after the OT) the performance of the system
466 in predicting the event impact is very high: in the area of 40 km radius around the epicenter, that
467 impacted an Intensity MCS VIII-IX as estimated by INGV shakemap), all 42 instrumented sites except
468 one showed a successful alert with only one false alarm. Considering the calculated blind-zone of
469 6.5 km radius, there is still a wide annular area, where the alert could have reached the population

before the strong ground shaking occurrence.

In Figure 5c, the circular blind-zone and lead-times are calculated at T_{FA}=3.65 sec which corresponds to the time of the P-waves detected at the first two stations, and when the first location, magnitude estimations and peak amplitudes are available. According to this simulation, only 1 municipality of the 170 located within 55 km of the epicenter and belonging to the regions of Abruzzo, Marche, Umbria and Lazio, would be located within the blind-zone. For these 2 municipalities the minimum negative lead-time is -0.5 sec at the town of Norcia, i.e., half-second is the maximum time in advance of the S-wave arriving at these sites before the alert issuing.

Even considering a later first alert, i.e., at 5.15 sec after the OT, the calculated blind-zone radius would have been 15 km long. 165 municipalities, located in the 15-55 km circular ring around the epicenter show positive lead-times, and might have been alerted 2 to 14.5 sec in advance to the arrival of the first S-wave at those sites.

At T_{FA}=3.65 sec, for 26 of the 60 accelerometric station sites, located at epicentral distances between 25 and 550 km, the EEW system incorrectly predicts a PGV below the threshold (e.g. a missed alert, MA). The numbers of MA at T_{FA}=3.65 sec for distant sites is mainly due to the underestimated PGV predicted by the GMPE with an initial lower magnitude as evaluated from near-source stations while using short P-wave time windows. As the time increases, larger portions of the P-wave time window are considered for the analysis and sites previously labelled as MA or SNA evolve towards SA and FA, respectively, with a final picture where only successful and false alerts are declared at the network. This is a common characteristic of similar time-evolutive EEWS that naturally tend with time to increase SA and FA at the expenses of MA and SNA.

This effect can be explained starting from the definitions of SA, SNA, MA and FA, provided by equations 9a, d. For each of the four possible situations, indeed, the second member of inequalities (related to I_{MM}^{obs}) does not change with time at the recording nodes. The first condition (related to the predicted intensity (I_{MM}^{pred}), instead, may evolve with time. Specifically, the instrumental intensity

is continuously predicted from the vertical P_x amplitude and, by definition of the P_x parameter, it can only increase or remain stable with time, so that once the predicted intensity has exceeded the threshold for warning declaration, the alert cannot be cancelled. With this in mind, the prediction performance at any recording sites may potentially evolve with time from SNA (light green) to FA (yellow) or from MA (red) to SA (dark green). Other transitions between alert states are, de facto, not possible.

Indeed, initial PGV underestimations leading to MA and SNA can be related to P-window lengths shorter than the half-duration of the earthquake source time function (*Colombelli and Zollo* [2015]) resulting in an initial magnitude underestimation. As the P-window time increases, since the max P-peak amplitude can only increase, the MAs can be confirmed or evolve in Successful Alerts, if the predicted PGV becomes larger than the threshold.

On the other hand, SNAs can be confirmed or, if the predicted PGV increases, can only evolve in False Alerts. With similar arguments, we note that, since the predicted PGV can only increase with an enlarged P-window, both all SAs and FAs would not change their status.

Building an EEW system that evolves with time in a manner that missed alerts and successful no-alerts tend to be minimized while increasing the number of successful alerts represent a strong advantage of the proposed EEWS, although this result is achieved at the expenses of an increase of false alerts. A similar conclusion was drawn by *Minson et al.* [2021] who analyzed the ideal case of a rail system in California's San Francisco Bay Area to explore potential uses of a network based EEW system for rail systems.

With this regard, we note that, at the first alert time and after, the relative percentage of SA, SNA, FA and MA critically depends on the predicted PGV (through the measured Px (eq.4)) and on the chosen IMM (or PGV) threshold, due to the natural distribution and scattering of data around the empirical laws that are used to predict PGV from the P-peak amplitude. This is clearly depicted in Figure S4, that shows an example of the used empirical attenuation relations between PGV and Pv.

For a given PGV threshold and a measured value of Pv, the diagram Predicted PGV vs measured P-amplitude is partitioned in 4 regions, around the predicted PGV point: the regions of SAs (dark-green, top-right), SNAs (light-green, bottom-left), FA (yellow, bottom-right) and MA (red, top-left). It is clear how the relative proportion of SA, SNA, FA, and MA depends on the measured Px and selected PGV threshold, that can change with time as the Px value and associated predicted PGV increase. This example demonstrates that if PGV's predictions are based on empirical regressions of P-wave amplitude data, the perspective solution to improve the performance of the time-evolutive EW system is to refine the empirical PGV prediction laws. This will be possibly achieved using AI-based machine learning approaches or through the exploration of more complex multi-parametric regression models (which includes site, azimuthal, distance effects) than the ones represented by eq. 4.

Conclusions

We have proposed an EEW method which uses the real-time P-peak amplitudes progressively measured at a dense accelerometric network around the epicenter to track the time-evolving potential damage zone, i.e., the area within which the strong ground motion is expected to exceed a given instrumental intensity threshold. Compared with source-based early warning approaches, where the event magnitude and location are used to issue an alert, our method follows an impact-based strategy, where the alert is rather issued upon the prediction of the strong ground shaking amplitudes at sites to be secured during the earthquake emergency. The method is time-evolutive, since the shape of the potential damage zone is modeled according to new data incoming from progressively distant stations and larger P-wave windows are assimilated by the EW system. The potential damage zone is traced by combining the Peak Ground Velocity values predicted by early P-wave amplitudes at accelerometer sites with values predicted by the regional GMPE using the updated values of location and moment magnitude.

We showed that the P-wave-based, early shake-map well reproduce the elongation and shape of the

final shake-map and the extent of the area driven by the rupture directivity and that suffered the largest shaking and damage during the October 30, 2016, M 6.5 Central Italy event.

The offline simulation of the EW method illustrates a common characteristic of time-evolutive EW systems, i.e. while trying to reduce uncertainties as much as possible, it will not be possible to eliminate the occurrence of false and missed alarms, so it is necessary for the end-user to accept these eventualities and account for them in a probabilistic frame to be implemented in a user-specific, decision-making strategy for minimizing the earthquake impact in real-time.

Despite these intrinsic limitations, a time-evolutive EEW as the one illustrated in our study, can significantly mitigate earthquake losses for false alert-tolerant users, who set the threshold and time of the alerts based on their specific mitigation actions, thus averaging between the requirement of the system to be fast in alerting (long lead-times) and accurate in the shaking predictions (reduced number of missed and false alarms).

References

Allen, R.M., Melgar, D., 2019. Earthquake Early Warning: Advances, Scientific Challenges, and Societal Needs. Annu. Rev. Earth Planet. Sci. 47, 361–388. https://doi.org/10.1146/annurev-earth-053018-060457

Allen, R. M., and A. Ziv (2011), Application of real-time GPS to earthquake early warning, Geophys. Res. Lett., 38, L16310, doi:10.1029/2011GL047947

Allen RM, Gasparini P, Kamigaichi O, Böse M. 2009. The status of earthquake early warning around the world: an introductory overview. Seismol. Res. Lett. 80(5):682–93

Bindi,D. Pacor, F., Luzi, L., Puglia, R., Massa, M., Ameri, G. and R. Paolucci (2011) Ground motion prediction equations derived from the Italian strong motion database. Bull Earthquake Eng (2011) 9:1899–1920, DOI 10.1007/s10518-011-9313-z

569 Boore, David & Stephens, Chris & Joyner, William. (2002). Comments on baseline correction of
570 digital strong-motion data: examples from the 1999 Hector Mine, California, earthquake. Bulletin
571 of the Seismological Society of America. 92. 1543-1560.
572 Böse, M., Thomas H. Heaton, Egill Hauksson (2012) Real-time Finite Fault Rupture Detector
573 (FinDer) for large earthquakes, Geophysical Journal International, Volume 191, Issue 2, November,
574 Pages 803–812, https://doi.org/10.1111/j.1365-246X.2012.05657.x
575 Cheloni, D., et al. (2017), Geodetic model of the 2016 Central Italy earthquake sequence inferred
576 from InSAR and GPS data, Geophys. Res. Lett., 44, 6778–6787, doi:10.1002/2017GL073580
577 Colombelli, S., Zollo, A., Festa, G. & Kanamori, H.(2012) Early magnitude and potential damage
578 zone estimates for the great Mw 9 Tohoku-Oki earthquake. Geophys. Res. Lett. 39, L22306.
579 Colombelli, S., R. M. Allen, and A. Zollo (2013), Application of real-time GPS to earthquake early
580 warning in subduction and strike-slip environments, J. Geophys. Res. Solid Earth, 118,
581 doi:10.1002/jgrb.50242
582 Colombelli, S., A. Zollo, G. Festa, and M. Picozzi (2014), Evidence for a difference in rupture
583 initiation between small and large earthquakes, Nat. Commun., 5, 3958,
584 doi:10.1038/ncomms4958.
585 Colombelli, S., Caruso, A., Zollo, A., Festa, G. and Kanamori, H. (2015), A P wave-based, on-site
586 method for earthquake early warning. Geophys. Res. Lett., 42: 1390– 1398. doi:
587 10.1002/2014GL063002
588 Colombelli, S., and A. Zollo (2015) Fast determination of earthquake magnitude and fault extent
589 from real-time P-wave recordings, Geophysical Journal International, Volume 202, Issue 2, , Pages
590 1158–1163, https://doi.org/10.1093/gji/ggv217
591 Colombelli, Simona & Festa, Gaetano & Zollo, Aldo. (2020). Early rupture signals predict the final
592 earthquake size. Geophysical Journal International. 223. 692-706. 10.1093/gji/ggaa343.
593 Caruso, A., S. Colombelli, L. Elia, M. Picozzi and A. Zollo, (2017) An onsite alert level early warning

system for Italy, J. Geophys. Res. Solid Earth, 122, doi 10.1002/2016JB013403

Clinton J, Zollo A,Marmureanu A, Zulfikar C, Parolai S. 2016. State-of-the art and future of earthquake early warning in the European region. Bull. Earthq. Eng. 14(9):2441–58

Faenza L. and A. Michelini, (2010). Regression analysis of MCS intensity and ground motion parameters in Italy and its application in ShakeMap, Geophysical Journal International, Volume 180, Issue 3, March 2010, Pages 1138–1152, https://doi.org/10.1111/j.1365-246X.2009.04467.x

Gruppo di Lavoro INGV sul terremoto in centro Italia (2016). Rapporto di sintesi sul Terremoto in centro Italia Mw 6.5 del 30 ottobre 2016, doi: 10.5281/zenodo.166019 (in Italian).

Grapenthin, R., Johanson, I. A., and Allen, R. M. (2014), Operational real-time GPS-enhanced earthquake early warning, J. Geophys. Res. Solid Earth, 119, 7944– 7965, doi:10.1002/2014JB011400.

Kanamori H. Real-time seismology and earthquake damage mitigation. Ann Rev Earth Planet Sci 2005;33:195–214, doi:10.1146/annurev.earth. 33.092203.122626.

Kodera, Y., Yasuyuki Yamada, Kazuyuki Hirano, Koji Tamaribuchi, Shimpei Adachi, Naoki Hayashimoto, Masahiko Morimoto, Masaki Nakamura, Mitsuyuki Hoshiba (2018) The Propagation of Local Undamped Motion (PLUM) Method: A Simple and Robust Seismic Wavefield Estimation Approach for Earthquake Early Warning. *Bulletin of the Seismological Society of America* , 108 (2): 983–1003. doi: https://doi.org/10.1785/0120170085

Lomax, A., J. Virieux, P. Volant and C. Berge, 2000. Probabilistic earthquake location in 3D and layered models: Introduction of a Metropolis-Gibbs method and comparison with linear locations, in *Advances in Seismic Event Location* Thurber, C.H., and N. Rabinowitz (eds.), Kluwer, Amsterdam, 101-134..

Lomax, A., C. Satriano and M. Vassallo (2012), Automatic picker developments and optimization: FilterPicker - a robust, broadband picker for real-time seismic monitoring and earthquake early-warning, Seism. Res. Lett. , 83, 531-540, doi: 10.1785/gssrl.83.3.531

619 Luzi L., Puglia R, Russo E & ORFEUS WG5 (2016). Engineering Strong Motion Database, version 1.0.
620 Istituto Nazionale di Geofisica e Vulcanologia, Observatories & Research Facilities for European
621 Seismology. doi: 10.13127/ESM
622 Minson, S.E., Baltay, A.S., Cochran, E.S. et al. The Limits of Earthquake Early Warning Accuracy and
623 Best Alerting Strategy. Sci Rep 9, 2478 (2019). https://doi.org/10.1038/s41598-019-39384-y
624 Nakamura Y, Tucker BE. 1988. Japan's earthquake warning system: should it be imported to
625 California? Calif. Geol. 41(2):33–40
626 Minson, S.E., Cochran, E.S., Wu, S., Noda, S. (2021). A Framework for Evaluating Earthquake Early
627 Warning for an Infrastructure Network: An Idealized Case Study of a Northern California Rail
628 System. Front. Earth Sci. 9, 620467. https://doi.org/10.3389/feart.2021.620467
629 Nazeri, S., Colombelli, S. & Zollo, A. (2019), "Fast and accurate determination of earthquake
630 moment, rupture length and stress release for the 2016-2017 Central Italy seismic sequence",
631 Geophysical Journal International, Volume 217, Issue 2, Pages 1425–1432,
632 doi.org/10.1093/gji/ggz097
633 Scognamiglio, L., Tinti, E., Casarotti, E., Pucci, S., Villani, F., Cocco, M., et al. (2018). Complex fault
634 geometry and rupture dynamics of the MW 6.5, 30 October 2016, central Italy earthquake. Journal
635 of Geophysical Research: Solid Earth, 123, 2943– 2964. https://doi.org/10.1002/2018JB015603
636 Satriano, C., Lomax, A., Zollo, A. (2008). Real-Time Evolutionary Earthquake Location for Seismic
637 Early Warning. Bulletin of the Seismological Society of America, 98 (3): 1482–1494.
638 https://doi.org/10.1785/0120060159
639 Trugman, D. T., Page, M. T., Minson, S. E., & Cochran, E. S. (2019). Peak ground displacement
640 saturates exactly when expected: Implications for earthquake early warning. Journal of
641 Geophysical Research: Solid Earth, 124, 4642– 4653. https://doi.org/10.1029/2018JB017093
642 Worden, C. B., Wald, D. J., Allen, T. I. ,Lin, K. Garcia, D. and G. Cua; A Revised Ground-Motion
643 and Intensity Interpolation Scheme for ShakeMap (2010) *Bulletin of the Seismological Society of*

644 *America* 100 (6): 3083–3096. doi: https://doi.org/10.1785/0120100101

645 Wu, Y. M., and H. Kanamori (2005), Experiment of an on-site method for the Taiwan Early Warning

646 System, Bull. Seismol. Soc. Am., 95, 347–353, doi:10.1785/0120040097

647 Wu, Y.-M., and L. Zhao (2006), Magnitude estimation using the first three seconds P-wave

648 amplitude in earthquake early warning, Geophys. Res. Lett.,33,L16312,

649 doi:10.1029/2006GL026871

650 Zollo, A., Amoroso, O. , Lancieri, M. , Wu, Y. And H. Kanamori (2010). A Threshold-based

651 Earthquake Early Warning using dense accelerometer networks. Geophysical Journal International.

652 183. 10.1111/j.1365-246X.2010.04765.x.

653 Zollo, A., Lancieri, M. & Nielsen, S. (2006) Earthquake magnitude estimation from peak amplitudes

654 of very early seismic signals on strong motion. Geophys. Res. Lett. 33, L23312,

655 https://doi.org/10.1029/2006GL027795 (2006)

656 Zollo, A., Nazeri,S. and S. Colombelli,(2021a) Earthquake Seismic Moment, Rupture Radius, and

657 Stress Drop From P-Wave Displacement Amplitude Versus Time Curves, *IEEE Transactions on*

658 *Geoscience and Remote Sensing*, vol. 60, pp. 1-11, 2022, Art no. 5912211, doi:

659 10.1109/TGRS.2021.3119909.

660 Zollo, A., Caruso, A., De Landro, G., Colombelli, S., & Elia, L. (2021b). A Bayesian method for real-

661 time earthquake location using multiparameter data. *Journal of Geophysical Research: Solid Earth*,

662 126, e2020JB020359. https://doi.org/10.1029/2020JB020359

663

664

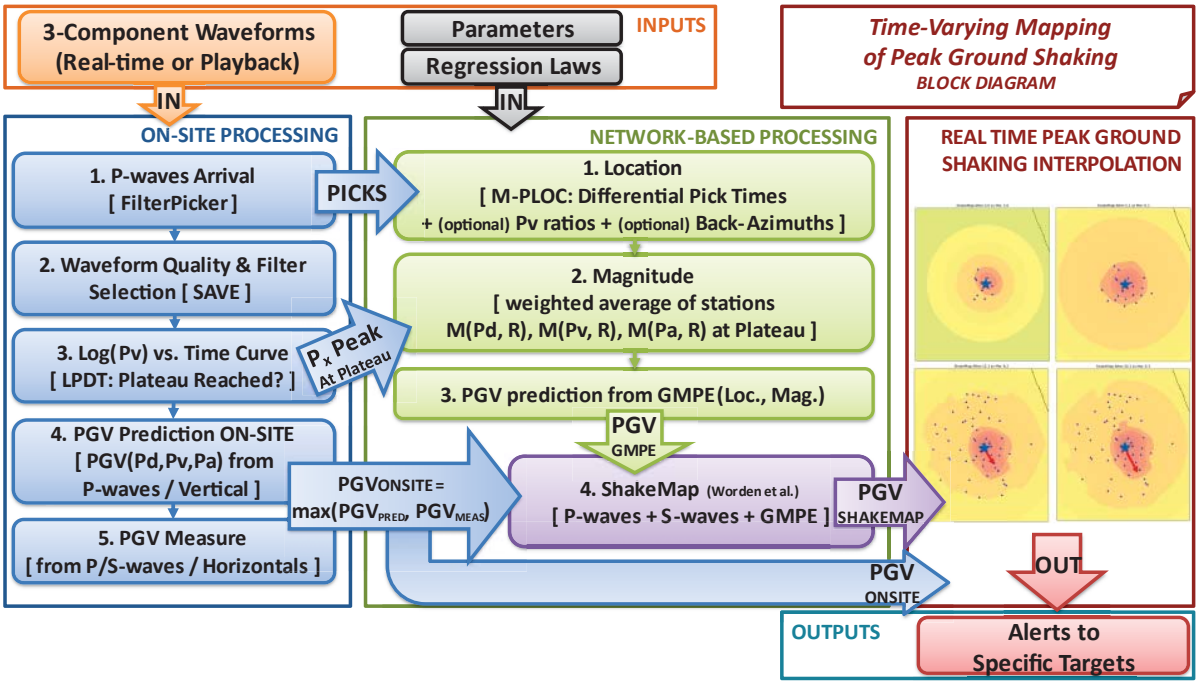

Figure 1: Block Diagram of the method. The figure shows the block diagram of the methodology, in which on-site PGV predictions (left) are combined with network-based PGV predictions (center), for a refined, real-time shake map construction and dissemination of alerts at target sites (right).

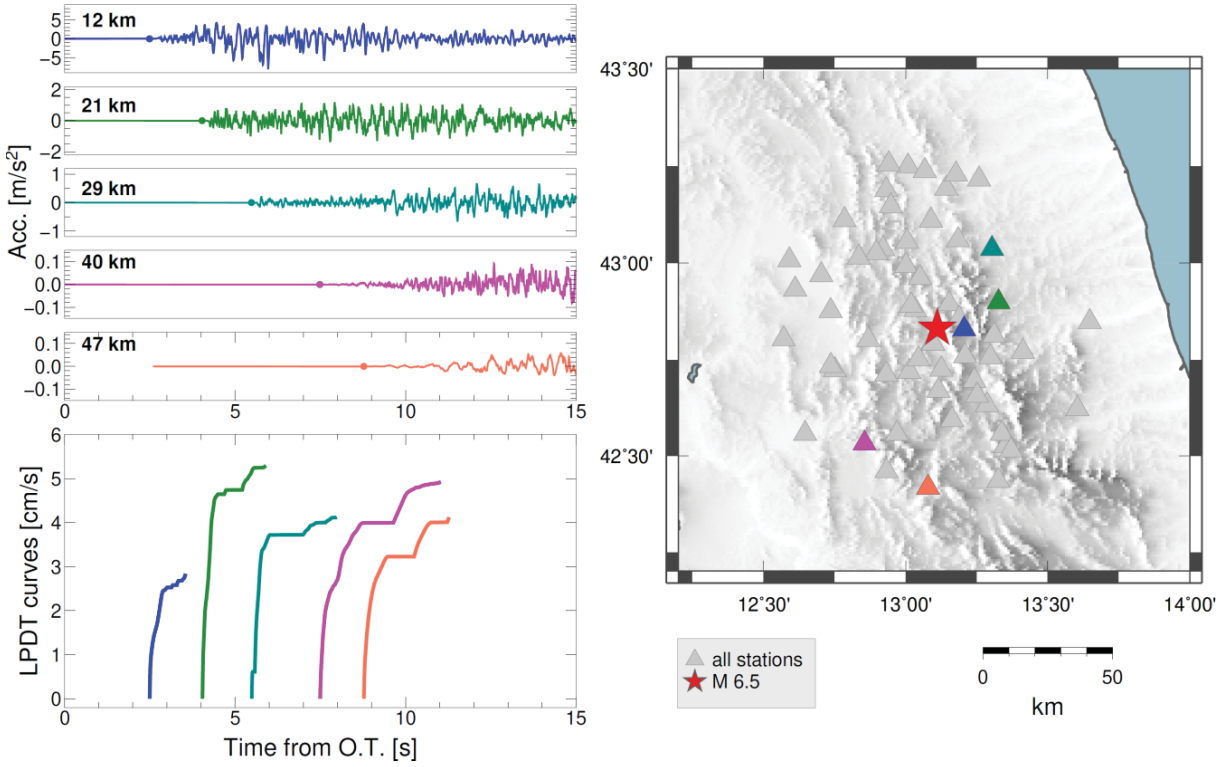

Figure 2: Example of seismograms and LPDT curves. a) Examples of acceleration records at increasing distance from the source (from top to bottom). Colors are used to identify the corresponding stations in panels b) and c) and for each station, the hypocentral distance is reported on the plot. b) LPDT curves computed at each station, starting at the P-wave arrival (shown with a coloured circle on each seismogram) and stooping at the expected arrival of S-waves. For a matter of visualization, the LPDT curves are initialized to a common, amplitude value. c) Map of the epicentral position of the earthquake and recording stations within a maximum distance of 50 km.

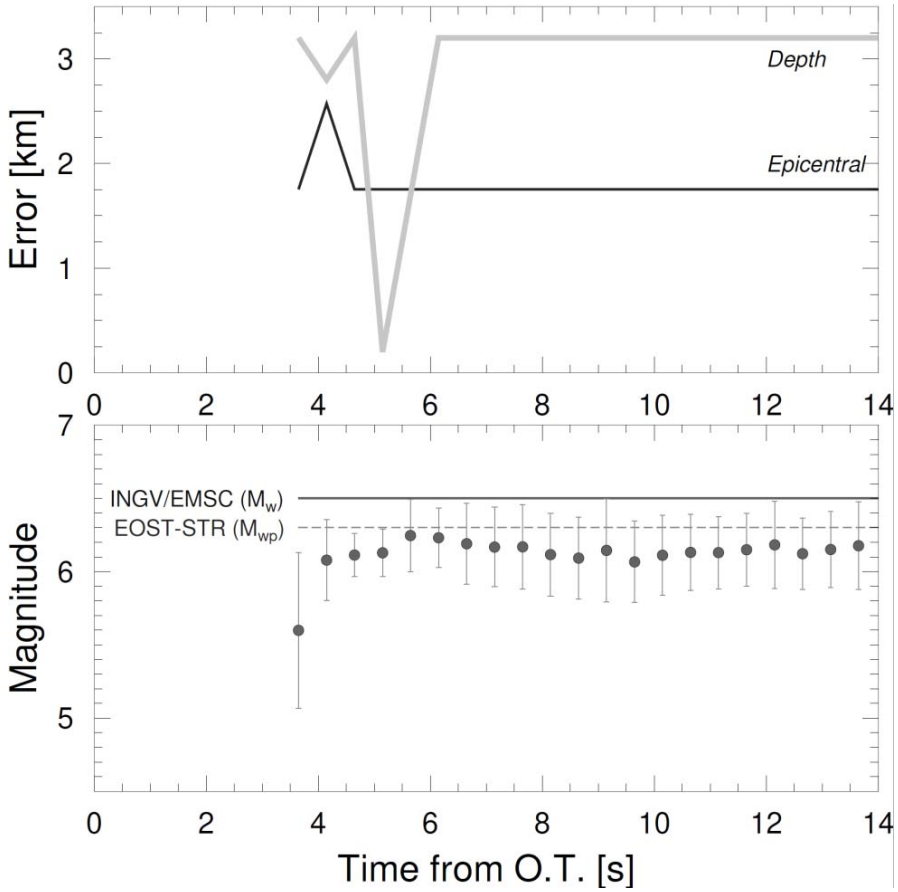

Figure 3: Time-evolutive estimation of event location and magnitude. The plot shows the comparison between the real-time earthquake location (top panel) with the bulletin solution, both for the epicentral position (black line) and for the earthquake depth (grey line). The bottom panel shown the real-time estimate of the earthquake magnitude, as average values (gray circles) and their uncertainties (error bars). Magnitude estimates form available agencies are also shown for reference, with horizontal lines. In both panels, the x-axis shows time in seconds form the origin time of the event.

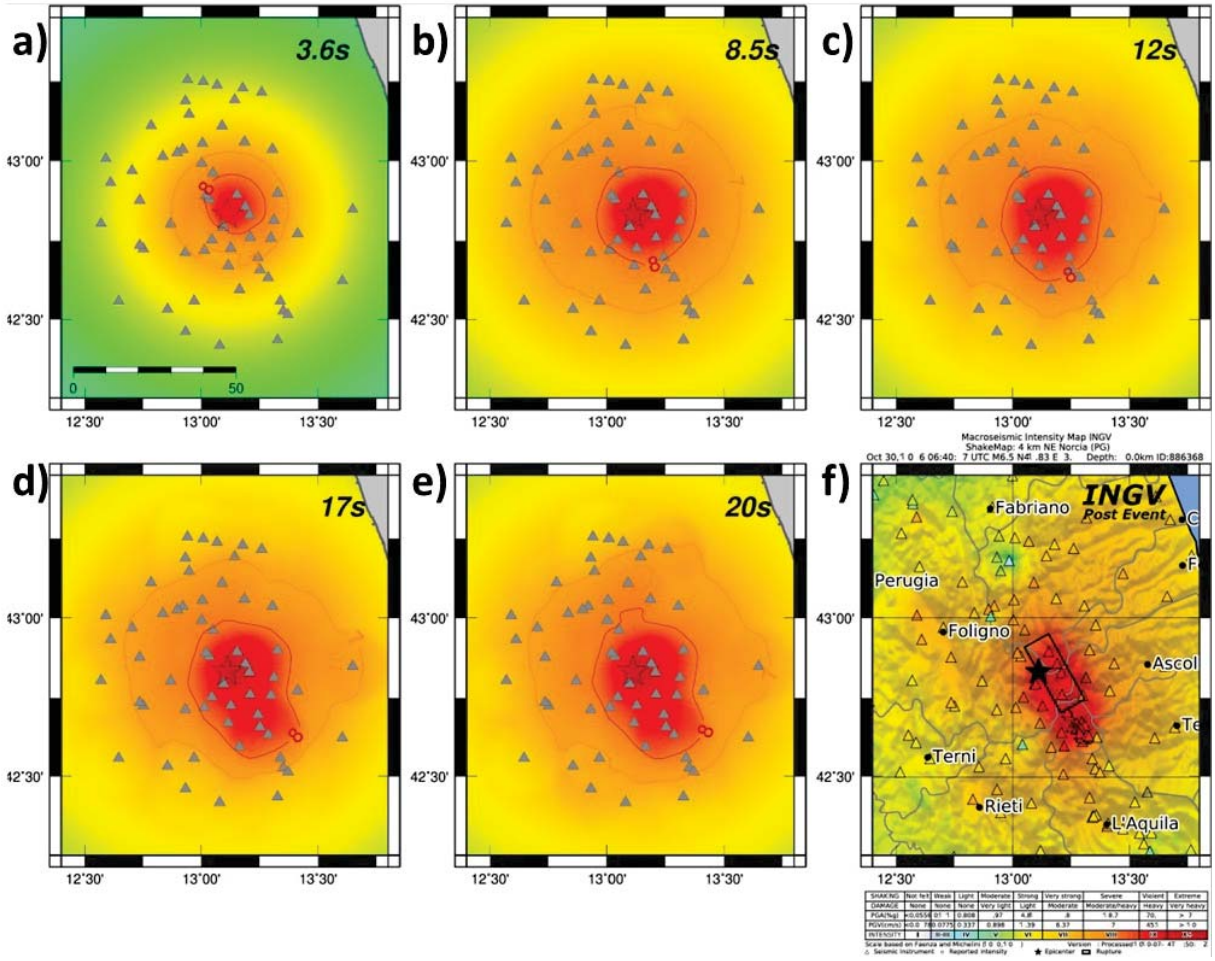

Figure 4: Results for the 2016-10-30, Mw 6.5, Norcia (Italy) Earthquake. Examples of the evolutionary, P-wave based early shake maps at different seconds from origin time (reported in each panel). In each panel, stations are the gray triangles, the red star is the epicenter of the event and the contour lines for the predicted intensity levels VII and VIII are also shown. The bottom-right panel is the reference INGV shake map.

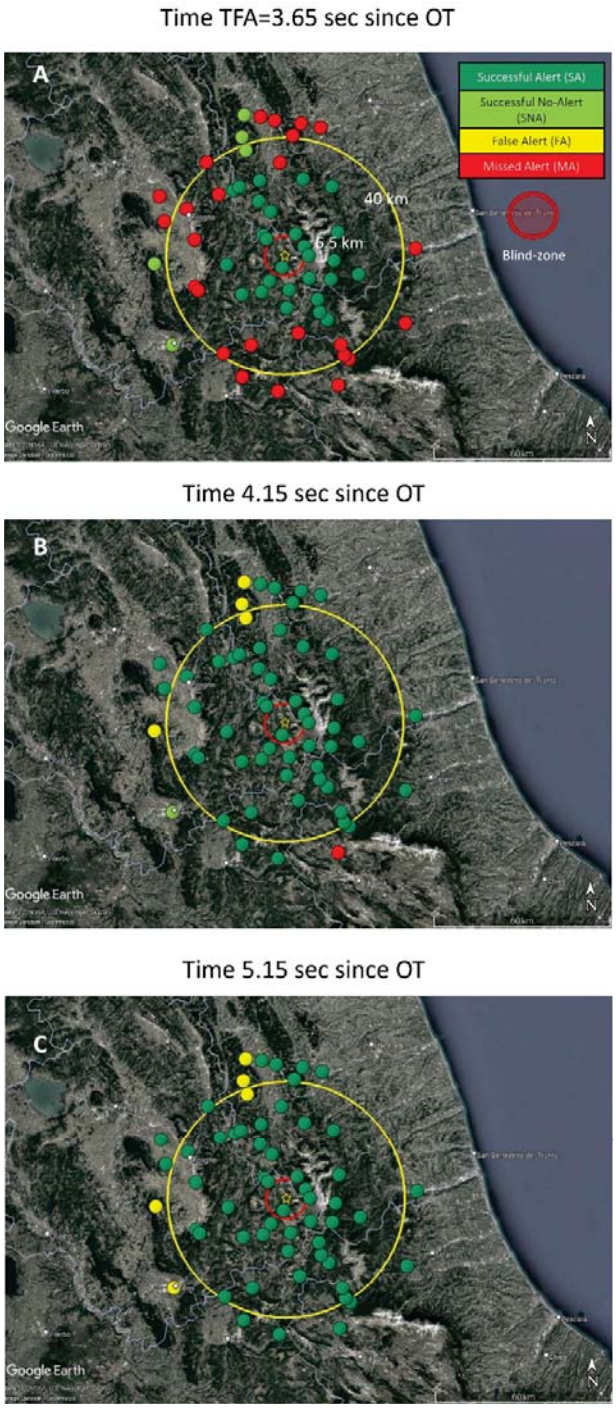

Figure 5: Performance Evaluation. The figure shows the performance of the system at the three different times in terms of Successful Alerts (dark green), Successful No-Alerts (light green), Missed Alerts (red) and False Alerts (yellow) at each station position. In all panels, the yellow circle is the 40km radius around the epicenter, while the red circle represents the blind zone.

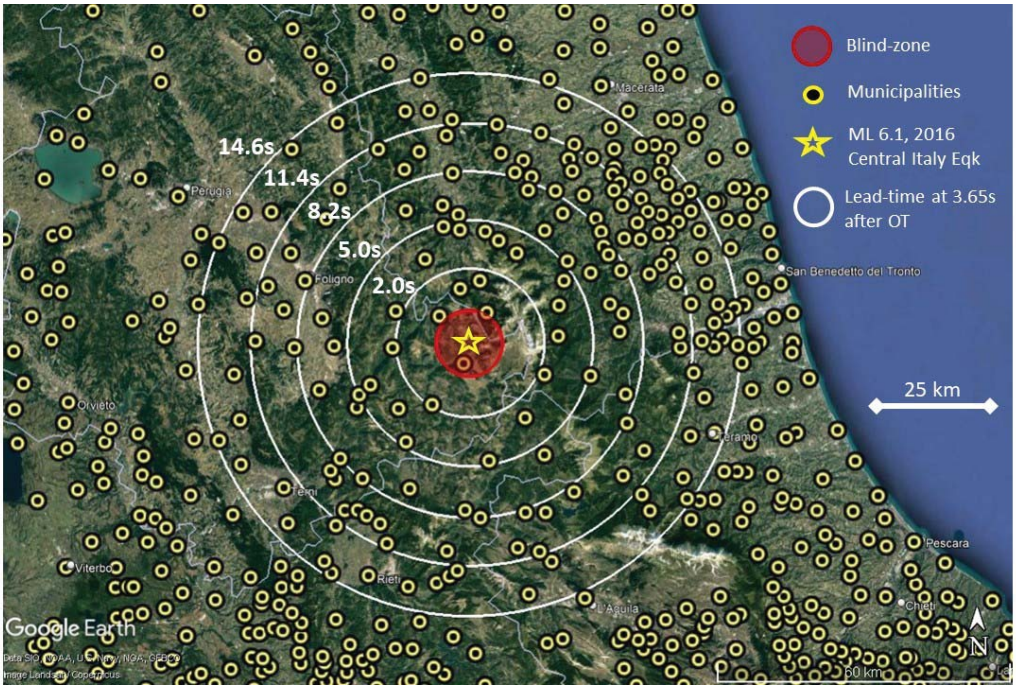

Figure 6: Lead-Time map. The figure shows values the map of available lead-times in the epicentral area and the position of municipalities that could have benefit from the warning. Each circle on the map represents the area in which the corresponding lead-time (indicated in white) would have been available.

.